 CMES, vol.95, no.2, pp.87-118, 2013

Brittle Fracture and Hydroelastic Simulations based on Moving Particle Simulation

R.A. Amaro Junior[1] **and L.Y. Cheng**[1]

Abstract: In this paper simulations of brittle fracture and hydroelastic problems are carried out by using a numerical approach based on the Moving Particle Simulation (MPS) method. It is a meshless method used to model both fluid and elastic solid, and all the computational domain is discretized in Lagrangian particles. A higher order accuracy gradient operator is used herein by adopting a correction matrix. Also, in order to correctly simulate the collision of the fragments, a contact detection algorithm that takes into account the presence of the solid surfaces generated by brittle fracture is proposed. In case of fluid-structure interaction, a partitioned coupling between fluid and isotropic elastic solid is adopted. Explicit and semi-implicit time integration algorithms are used for elastic solid and fluid domains, respectively. Matching of the time steps in both domains is done by subcycling technique to improve the computational efficiency. The performance of method is evaluated by analyzing the results of several cases of study. At first, the dynamics of slender cantilever beam is analyzed to check the convergence of the method. After that, a collision between two elastic solids with brittle fracture and further collision between the fragments is simulated to show the improvement achieved. Finally, to validate the fluid-structure interaction simulation approach, comparison with available numerical results of a dam breaking on an elastic plate is performed, as well as the comparison with available experimental measurements of the interaction between liquid sloshing and an elastic plate.

Keywords: Fluid-structure interaction, brittle fracture, elastic solid, moving particle simulation, particle method, hydroelasticity.

1 Introduction

Over the last 50 years, numerical simulation enabled the study of complex physical systems in several areas of sciences and engineering. The most commons meth-

[1] Department of Construction Engineering, Polytechnic School, University of São Paulo, São Paulo, SP, Brazil.

ods are the Finite Difference Method (FDM), Finite Volume Method (FVM), Finite Element Method (FEM) and Boundary Element Method (BEM). However, generally these mesh-based methods face several restrictions when the problems involve large deformation or displacement of the boundaries, such as free surface, fragmentation, merging or multibody interactions, and ingenious boundary tracking or remeshing techniques are required, increasing the computational complexity. Due the easy implementation and flexibility, the meshless methods has attracted much attention in recent years. An important class of meshless method are the particle-based methods, where the behavior of a physical problem is represented by a collection of points (particles). In a particle method each particle moves accordingly with its own mass and the internal/external forces evaluated by the interaction with the neighboring particles [Idelsohn and Onate (2006)]. Examples of particle methods utilized in different field of sciences and engineering are: Particle in Cell (PIC) [Harlow (1964)], Smooth Particle Hydrodynamics (SPH) [Lucy (1977); Gingold and Monagham (1977)], Material Point Method (MPM) [Sulsky, Chen, and Schreyer (1994)], Moving Particle Semi-implicit (MPS) [Koshizuka, Tamako, and Oka (1995)] and Particle Finite Element Method (PFEM) [Idelsohn, Onate, and Pin (2004)].

In the recent years, problems involving dynamic flexible bodies and their interaction with free surface flow have received great attention in several field of engineering and science. Nevertheless, their computational modeling remains as a great challenge.

Regarding the fracture phenomenon, it is governed by interaction of micro and macro-voids, microstructural defects and initial flaws, and involve multiple physical processes occurring at different time and length scales [Das and Cleary (2010)]. Generally, when investigating fracture problems using mesh-based methods, several shortcomings, such as the impossibility of crack propagation along the element's edge and mesh distorting may occur. To overcome the constraints imposed by mesh, particle methods have been proposed to model the fracture phenomenon. For example, Guo and Nairn (2006) described algorithms for three-dimensional dynamic stress and fracture analysis using MPM. Das and Cleary (2010) used SPH to modeling breakage of rocks under impact, common in many industrial processes. Xiao, Han, and Hu (2011) presented a FEM-SPH coupling algorithm and proposed an adaptive coupling technique to simulate impact problems involving large deformations and fractures. Chen, Wang, Xie, and Qin (2013) presented a hybrid approach based on SPH for rapid crack simulation of brittle material in physics-based animation area.

On the other hand, in the case of fluid-structure interaction (FSI) problems, a coupling strategy to satisfy both the geometrical compatibility and the equilibrium con-

ditions on the interface is a key issue [Ishihara and Yoshimura (2005)]. The main approaches employed in the solution of FSI problems are roughly divided into the monolithic methods, in which fully coupled fluid-structure interaction in the interface is handled synchronously, and the partitioned methods, in which the equations of fluid and structure are alternately integrated in time, and interface conditions are handled asynchronously. For numerical simulations of hydroelastic problems involving free surface, the Lagrangian formulation have been widely used, especially numerical approach based on particle methods. Idelsohn, Onate, and Pin (2004) modeled interactions between floating and submerged bodies and free surface flows by using PFEM. Antoci, Gallati, and Sibilla (2007) studied experimentally and numerically based on SPH method, the deformation of an elastic plate under the effect of a rapidly varying fluid flow. Campbell, Vignjevic, Patel, and Milisavljevic (2009) presented a explicit SPH-finite element approach to simulate floating body, and showed the ability of the numerical approach to represent large structural deformation due to water impact.

Within this context and to take advantage of particle methods, a practical computational technique for modeling and simulation of brittle fracture and hydroelastic problems is presented in this paper.

The numerical approach is based on the Moving Particle Simulation (MPS) method, in which all the computational domain, including solid and fluid, is discretized in Lagrangian particles. Due to fully Lagrangian description, numerical diffusion caused by advection term does not arise. As a meshless method, it is very effective for the simulation of problems involving complex deformations of the boundaries and has been widely applied in several engineering problems, for example: Nonlinear hydrodynamics such as green water [Shibata, Koshizuka, Sakai, and Tanizawa (2012); Bellezi, Cheng, and Nishimoto (2013)], sloshing [Lee, Jeong, Hwang, Park, and Kim (2013)], coupled motion of sloshing and vessel [Lee, Park, Kim, and Hwang (2011); Kim, Lee, Kim, and Park (2011)], and sloshing motion coupled to a moving suppression device [Tsukamoto, Cheng, and Nishimoto (2011)]; Multiphase flows [Koshizuka, Ikeda, and Oka (1999); Park and Jeun (2011); Cheng, Gomes, Yoshino, and Nishimoto (2011)]; Elastic solid [Chikazawa, Koshizuka, and Oka (2001); and other industrial problems [Kakuda, Ushiyama, Obara, Toyotani, Matsuda, Tanaka, and Katagiri (2010); Cheng, Oliveira, Favero, Oliveira, and Gonçalves (2013); Motezuki and Cheng (2013)] and biomedical engineering applications [Chhatkuli, Koshizuka, and Uesaka (2009); Nagayama and Honda (2012)].

In the present paper, a higher order accuracy gradient operator is used as an attempt to improve the accuracy. Also, in order to correctly simulate the collision of the fragments, a simple condition of brittle fracture associated to a more generic contact detection algorithm that takes into account the presence of the solid surfaces

generated by brittle fracture is proposed. To solve hydroelastic problems involving free surface, a partitioned coupling between fluid and isotropic elastic solid is adopted. The solid surface particles are treated like a fluid particle and the pressures of the solid surface particles are computed by solving Poisson equation for the pressure, together with the fluid particles. Therefore, the coupling between solid and fluid is done at first by using the displacement and velocity of elastic solid as the boundary conditions for the fluid domain. Then the pressure on the solid surface particles is obtained by solving the fluid motion. After that the calculated pressure field is taken into account in the calculation of the motion of the elastic solid. Explicit and semi-implicit time integration algorithms are used for elastic solid and fluid domains, respectively. Matching of the time steps in both domains is done by sub-cycling technique to improve the computational efficiency.

In the next sections, a brief description of the MPS model for both fluid and elastic solid is presented, as well as the brittle fracture condition, the contact detection algorithm and the coupling technique between fluid and elastic solid. Finally, the performance of method is evaluated by simulations of several cases of study. At first, the dynamics of slender cantilever beam is analyzed to check the convergence of the method. After that, a collision between two elastic solids with brittle fracture and further collision between the fragments is simulated to show the improvement achieved. Finally, to validate the fluid-structure interaction simulation approach, comparison with available numerical results of a dam breaking on an elastic plate is performed, as well as the comparison with available experimental measurements of the interaction between liquid sloshing and an elastic plate.

2 Governing equations

2.1 Fluid

The governing equations of incompressible viscous flow are expressed by the conservation laws of mass and momentum:

$$\frac{D\rho}{Dt} + \rho(\nabla \cdot \boldsymbol{v}) = 0 \tag{1}$$

$$\frac{D\boldsymbol{v}}{Dt} = -\frac{1}{\rho}\nabla P + \nu\nabla^2\boldsymbol{v} + \boldsymbol{f} \tag{2}$$

where ρ is the density, $\boldsymbol{v}$ is the velocity vector, P is the pressure, ν is the kinematic viscosity, $\boldsymbol{f}$ is the external force vector.

2.2 Solid

For the dynamics analysis of elastic solids, the governing equation of motion can be written as:

$$\rho \frac{D\boldsymbol{v}}{Dt} = \nabla \cdot (2\mu\boldsymbol{\varepsilon} + \lambda tr(\boldsymbol{\varepsilon})\boldsymbol{I}) + \boldsymbol{b} \tag{3}$$

where $\boldsymbol{\varepsilon}$ is the strain tensor and $\boldsymbol{b}$ is the body force vector. The Lamé's constants μ and λ are given by:

$$\mu = \frac{E}{2(1+v)} \qquad \lambda = \frac{Ev}{(1+v)(1-2v)} \tag{4}$$

where E is the Young's modulus and v is the Poisson's ratio.

The Eq. 3, can be rewritten by introducing stress tensor $\boldsymbol{\sigma}$ and isotropic pressure p as:

$$\rho \frac{D\boldsymbol{v}}{Dt} = \nabla \cdot (\boldsymbol{\sigma} - p\boldsymbol{I}) + \boldsymbol{b} \tag{5}$$

where stress tensor and isotropic pressure are calculated as:

$$\boldsymbol{\sigma} = 2\mu\boldsymbol{\varepsilon} \qquad p = -\lambda tr(\boldsymbol{\varepsilon}) \tag{6}$$

3 Numerical model

In MPS method, the differential operators of the governing equations are replaced by discrete differential operators on irregular nodes [Isshiki (2011)], which are derived from a model of interaction between particles. For a given particle i, the influence of a neighbor particle j is defined by weight function $w(|\boldsymbol{r}_{ij}|)$ given in Eq. 7:

$$w(|\boldsymbol{r}_{ij}|) = \begin{cases} \frac{r_e}{|\boldsymbol{r}_{ij}|} - 1, & |\boldsymbol{r}_{ij}| \leq r_e \\ 0, & |\boldsymbol{r}_{ij}| > r_e \end{cases} \tag{7}$$

where r_e is the effective radius that limits the range of influence and $\boldsymbol{r}_{ij}$ is the distance between i and j. In the other words, r_e defines the neighborhood of the particle i.

The summation of the weight of all the particles in the neighborhood of the particle i is defined as its particle number density n_i:

$$n_i = \sum_{j \neq i} w(|\boldsymbol{r}_{ij}|) \tag{8}$$

As a result, for a scalar function ϕ and a vector function $\boldsymbol{\phi}$, the gradient, divergence, rotation and Laplacian operators can be defined by Eq. 9, Eq. 10, Eq. 11 and Eq. 12, respectively:

$$\nabla\phi_i = \frac{d}{n_i^0}\sum_{j\neq i}\frac{(\phi_j-\phi_i)}{|\boldsymbol{r}_j-\boldsymbol{r}_i|^2}(\boldsymbol{r}_j-\boldsymbol{r}_i)w(|\boldsymbol{r}_{ij}|) \tag{9}$$

$$\nabla\cdot\boldsymbol{\phi}_i = \frac{d}{n_i^0}\sum_{j\neq i}\frac{(\boldsymbol{\phi}_j-\boldsymbol{\phi}_i)\cdot(\boldsymbol{r}_j-\boldsymbol{r}_i)}{|\boldsymbol{r}_j-\boldsymbol{r}_i|^2}w(|\boldsymbol{r}_{ij}|) \tag{10}$$

$$\nabla\times\boldsymbol{\phi}_i = \frac{d}{n_i^0}\sum_{j\neq i}\frac{(\boldsymbol{\phi}_j-\boldsymbol{\phi}_i)\cdot\boldsymbol{s}_{ij}}{|\boldsymbol{r}_j-\boldsymbol{r}_i|}w(|\boldsymbol{r}_{ij}|) \tag{11}$$

$$\nabla^2\phi_i = \frac{2d}{\lambda_l n_i^0}\sum_{j\neq i}(\phi_j-\phi_i)w(|\boldsymbol{r}_{ij}|) \tag{12}$$

where d is the number of spatial dimensions, $\boldsymbol{s}_{ij}$ is a versor perpendicular to $\boldsymbol{r}_{ij}$ and n_i^0 is the initial value of n_i. In case of fluid, the initial value of n_i is independent to the particle so that n^0 can be used instead of n_i^0. Finally, λ_l is a correction parameter so that the variance increase is equal to that of the analytical solution, and is calculated by:

$$\lambda_l = \frac{\sum_{j\neq i}|\boldsymbol{r}_{ij}|^2 w(|\boldsymbol{r}_{ij}|)}{\sum_{j\neq i}w(|\boldsymbol{r}_{ij}|)} \tag{13}$$

Adopting correction technique, initially proposed for the SPH method [Bonet and Lok (1999)], the gradient operator (Eq. 9) can be improved by introducing a correction matrix $\boldsymbol{A}$:

$$\tilde{\nabla}\phi_i = \boldsymbol{A}\left[\frac{1}{n_i}\sum_{j\neq i}\frac{(\phi_j-\phi_i)}{|\boldsymbol{r}_j-\boldsymbol{r}_i|}\frac{(\boldsymbol{r}_j-\boldsymbol{r}_i)}{|\boldsymbol{r}_j-\boldsymbol{r}_i|}w(|\boldsymbol{r}_{ij}|)\right] \tag{14}$$

$$\boldsymbol{A} = \left[\frac{1}{n_i}\sum_{j\neq i}\frac{(\boldsymbol{r}_j-\boldsymbol{r}_i)}{|\boldsymbol{r}_j-\boldsymbol{r}_i|}\otimes\frac{(\boldsymbol{r}_j-\boldsymbol{r}_i)}{|\boldsymbol{r}_j-\boldsymbol{r}_i|}w(|\boldsymbol{r}_{ij}|)\right]^{-1} \tag{15}$$

For two-dimensional cases analyzed herein, r_e is set to $2.1l_0$ to calculate gradient, divergence and rotation operators and r_e is set to $4.0l_0$ to calculate Laplacian operator, where l_0 is the initial distance between two adjacent particles.

4 Solution algorithm

4.1 Algorithm for incompressible viscous flow

To solve the incompressible viscous flow, a semi-implicit algorithm is used in the MPS method. At first, predictions of the particle's velocity $\boldsymbol{v}_i^*$ and position $\boldsymbol{r}_i^*$ are carried out explicitly by using viscosity and external forces terms of the momentum conservation (Eq. 2) [Ikeda, Koshizuka, Oka, Park, and Sugimoto (2001)]:

$$\boldsymbol{v}_i^* = \boldsymbol{v}_i^n + \Delta t \left(\nu \nabla^2 \boldsymbol{v}_i^n + \boldsymbol{f}_i\right) \tag{16}$$

$$\boldsymbol{r}_i^* = \boldsymbol{r}_i^n + \Delta t \boldsymbol{v}_i^* \tag{17}$$

As the fluid density ρ is proportional to the particle number density n_i, by applying the conservation law of mass (Eq. 1), we have:

$$\nabla \cdot \boldsymbol{v}_i^{'} = -\frac{1}{\Delta t} \frac{\rho_i^{n+1} - \rho_i^*}{\rho^0} = -\frac{1}{\Delta t} \frac{n_i^{n+1} - n_i^*}{n^0} \tag{18}$$

where n_i^* is the particle number density calculated after the movement of particles in the first prediction step and the deviation of the velocity $\boldsymbol{v}_i^{'}$ is owing to the implicit pressure term in the momentum conservation equation:

$$\boldsymbol{v}_i^{'} = -\frac{\Delta t}{\rho} \nabla P_i^{n+1} \tag{19}$$

By substituting Eq. 18 into Eq. 19, and considered incompressible flow, i.e. $n_i^{n+1} = n_0$, the Poisson equation for the pressure can be written as:

$$\nabla^2 P_i^{n+1} = \frac{\rho}{\Delta t^2} \frac{n_i^0 - n_i^*}{n^0} \tag{20}$$

In this work, it is assumed that density is a linear function of pressure:

$$\frac{n_i^{n+1}}{n_0} = \frac{\rho_i^{n+1}}{\rho^0} = 1 + \frac{P_i^{n+1}}{\rho c^2} \tag{21}$$

where c is the sound velocity. By substituting Eq. 21 into Eq. 20, we have:

$$\nabla^2 P_i^{n+1} = \frac{\rho}{\Delta t^2} \left(\frac{n_i^0 - n_i^*}{n^0} + \alpha P_i^{n+1} \right) \tag{22}$$

where $\alpha = 1/(\rho c^2)$.

Assuming a weakly compressible model of the Eq. 22, the numerical solution of the system of equation is faster than the Eq. 20 in each time step, improving the computational efficiency. Compared with incompressible results, the weakly compressible

condition has a neglectable effect on the accuracy of the results [Shakibaeinia and Jin (2010)].

Also, as the pressure computational is relatively sensitive to small variation of n_i^*, a relaxation coefficient κ is used for improving stability of a computation method and Eq. 22 is rewritten as:

$$\nabla^2 P_i^{n+1} - \alpha P_i^{n+1} = \kappa \frac{\rho}{\Delta t^2} \frac{n_i^0 - n_i^*}{n^0} \tag{23}$$

The value of $\kappa = 0.01$ is used in this study.

From Eq. 19, the velocity $\boldsymbol{v}_i^{n+1}$ of a particle i is updated and the position $\boldsymbol{r}_i^{n+1}$ can be obtained by:

$$\boldsymbol{r}_i^{n+1} = \boldsymbol{r}_i^n + \Delta t \boldsymbol{v}_i^{n+1} \tag{24}$$

4.2 Algorithm for elastic solid

For elastic solid, an explicit algorithm is used in the MPS method [Chikazawa, Koshizuka, and Oka (2001)]; [Song, Koshizuka, and Oka (2003)]. First the displacement vector $\boldsymbol{u}_{ij}$ between particles i and its neighbor j is calculated by:

$$\boldsymbol{u}_{ij} = \boldsymbol{r}_{ij} - \boldsymbol{R}_{ij} \boldsymbol{r}_{ij}^0 \tag{25}$$

where $\boldsymbol{R}_{ij}$ is the rotation matrix and $\boldsymbol{r}_{ij}^0$ the initial position vector.

The displacement vector can be divided into normal $(\boldsymbol{u}_{ij})_n$ and shear $(\boldsymbol{u}_{ij})_s$ components:

$$(\boldsymbol{u}_{ij})_n = \frac{(\boldsymbol{u}_{ij} \cdot \boldsymbol{r}_{ij})}{|\boldsymbol{r}_{ij}|} \frac{\boldsymbol{r}_{ij}}{|\boldsymbol{r}_{ij}|} \tag{26}$$

$$(\boldsymbol{u}_{ij})_s = \boldsymbol{u}_{ij} - (\boldsymbol{u}_{ij})_n \tag{27}$$

Thus the normal $\boldsymbol{\varepsilon}_{ij}$ and shear $\boldsymbol{\gamma}_{ij}$ strain vectors can be calculated by:

$$\boldsymbol{\varepsilon}_{ij} = \frac{(\boldsymbol{u}_{ij})_n}{|\boldsymbol{r}_{ij}^0|} \tag{28}$$

$$\boldsymbol{\gamma}_{ij} = \frac{(\boldsymbol{u}_{ij})_s}{|\boldsymbol{r}_{ij}^0|} \tag{29}$$

The volumetric deformation $tr(\boldsymbol{\varepsilon})$ is described using the divergence of displacement vector:

$$tr(\boldsymbol{\varepsilon}) = \nabla \cdot (\boldsymbol{u}_{ij}) = \frac{d}{n_i^0} \sum_{j \neq i} \frac{\boldsymbol{u}_{ij} \cdot \boldsymbol{r}_{ij}}{|\boldsymbol{r}_{ij}^0||\boldsymbol{r}_{ij}|} w(|\boldsymbol{r}_{ij}^0|) \tag{30}$$

From the strain vectors, the normal stress vector $\boldsymbol{\sigma}_{ij}$, shear stress vector $\boldsymbol{\tau}_{ij}$ and isotropic pressure p_i are calculated as:

$$\boldsymbol{\sigma}_{ij} = 2\mu\boldsymbol{\varepsilon}_{ij} \tag{31}$$

$$\boldsymbol{\tau}_{ij} = 2\mu\boldsymbol{\gamma}_{ij} \tag{32}$$

$$p_i = -\lambda tr(\boldsymbol{\varepsilon}) \tag{33}$$

For elastic solid, a modified differential operators is used in governing equation. A function ϕ is calculated in the intermediate position between two particles i and j, with the variable $\boldsymbol{r}_j$ replaced by $(\boldsymbol{r}_i + \boldsymbol{r}_j)/2$, and the gradient operator (Eq. 9) is rewriting as:

$$\nabla\phi_i = \frac{2d}{n_i^0}\sum_{j\neq i}\frac{\phi_{ij}}{|\boldsymbol{r}_j - \boldsymbol{r}_i|^2}(\boldsymbol{r}_j - \boldsymbol{r}_i)w(|\boldsymbol{r}_{ij}|) \tag{34}$$

where ϕ_{ij} is the function calculated in the intermediate position. Similar of the gradient operator, the divergence operator can be calculated by:

$$\nabla\cdot\boldsymbol{\phi}_i = \frac{2d}{n_i^0}\sum_{j\neq i}\frac{(\boldsymbol{\phi}_{ij})\cdot(\boldsymbol{r}_j - \boldsymbol{r}_i)}{|\boldsymbol{r}_j - \boldsymbol{r}_i|^2}w(|\boldsymbol{r}_{ij}|) \tag{35}$$

Applying Eq. 5, translation of particles can be obtained from divergence of the displacement (normal and shear stress vector) and isotropic pressure gradient:

$$\rho\left(\frac{\partial\boldsymbol{v}_i}{\partial t}\right)_n = \frac{2d}{n_i^0}\sum_{j\neq i}\frac{\boldsymbol{\sigma}_{ij}}{|\boldsymbol{r}_{ij}^0|}w(|\boldsymbol{r}_{ij}^0|) \tag{36}$$

$$\rho\left(\frac{\partial\boldsymbol{v}_i}{\partial t}\right)_s = \frac{2d}{n_i^0}\sum_{j\neq i}\frac{\boldsymbol{\tau}_{ij}}{|\boldsymbol{r}_{ij}^0|}w(|\boldsymbol{r}_{ij}^0|) \tag{37}$$

$$\rho\left(\frac{\partial\boldsymbol{v}_i}{\partial t}\right)_p = \frac{2d}{n_i^0}\sum_{j\neq i}\frac{p_{ij}}{|\boldsymbol{r}_{ij}^0|}\frac{\boldsymbol{r}_{ij}}{|\boldsymbol{r}_{ij}|}w(|\boldsymbol{r}_{ij}^0|) \tag{38}$$

where $p_{ij} = (p_i + p_j)/2$ is the average pressure.
Velocity $\boldsymbol{v}_i^{n+1}$ and position $\boldsymbol{r}_i^{n+1}$ of a particle i can be explicitly calculated as:

$$\boldsymbol{v}_i^{n+1} = \boldsymbol{v}_i^n + \Delta t\left[\left(\frac{\partial\boldsymbol{v}_i}{\partial t}\right)_n + \left(\frac{\partial\boldsymbol{v}_i}{\partial t}\right)_s + \left(\frac{\partial\boldsymbol{v}_i}{\partial t}\right)_p\right]^n \tag{39}$$

$$\boldsymbol{r}_i^{n+1} = \boldsymbol{r}_i^n + \Delta t\boldsymbol{v}_i^{n+1} \tag{40}$$

To ensure the conservation of angular moment, the force due the shear stress vector is taken in account for the rotation of particles, in order to cancel the torque between each pair of particles. The force can be calculated as Eq. 41 and the moment can be written as Eq. 42.

$$\boldsymbol{F}_{ij} = \frac{2d\ l_0^d}{n_i^0} \frac{\boldsymbol{\tau}_{ij}}{|\boldsymbol{r}_{ij}^0|} w(|\boldsymbol{r}_{ij}^0|) \tag{41}$$

$$\boldsymbol{M}_{ij} = -(\boldsymbol{r}_j - \boldsymbol{r}_i) \times \boldsymbol{F}_{ij} \tag{42}$$

If the moment of inertia I_i is constant along the time, the angular acceleration vector of particles can be calculated as:

$$I_i \frac{\partial \boldsymbol{\omega}_i}{\partial t} = -\frac{1}{2} \sum_{j \neq i} \boldsymbol{M}_{ij} \tag{43}$$

where the moment of inertia I_i is calculated as:

$$I_i = m\frac{l_0^2}{6} = \frac{\rho l_0^{2+d}}{6} \tag{44}$$

Finally, angular velocity $\boldsymbol{\omega}_i^{n+1}$ and rotation $\boldsymbol{\theta}_i^{n+1}$ of a particle i are explicitly calculated as:

$$\boldsymbol{\omega}_i^{n+1} = \boldsymbol{\omega}_i^n + \Delta t \left(\frac{\partial \boldsymbol{\omega}_i}{\partial t} \right)^n \tag{45}$$

$$\boldsymbol{\theta}_i^{n+1} = \boldsymbol{\theta}_i^n + \Delta t \boldsymbol{\omega}_i^{n+1} \tag{46}$$

4.3 Boundary Conditions

In order to identify free surface particles, the particle number density and the number of neighboring particles are used as checking parameters. A particle is defined as free surface particle and its pressure is set to zero when its particle number density n_i is smaller than $\beta_1 n^0$ and its number of neighboring particles is smaller than $\beta_2 N^0$, where N_0 is the number of neighboring particles inside the effective radius r_e in the initial distribution. The value of β_1 used in this study is 0.97 and β_2 is 0.85, based on Lee, Park, and Kim (2010). This double check technique improved the effectiveness of the free surface particle detection, which results in more stable computation of the fluid pressure.

Solid wall boundary condition is represented by three layers of fixed particles. The particles that form the layer in contact to the fluid are denominated wall particles,

of which the pressure is computed by solving Poisson equation for the pressure (Eq. 23), together with the fluid particles. The particles that forms two other layers are denominated dummy particles. Dummy particles are use to assure the correct calculation of the particle number density of the wall particles. Pressure is not calculated in the dummy particles.

As the boundary condition for a fixed end of elastic solid, the motions of the particles are constrained by setting the displacements to zero.

4.4 Brittle fracture

A simplified condition of brittle fracture is implemented in order to simulate multibody dynamics with rupture of brittle solids. When the strain ε_{ij} between particles i and j is greater than a critical value ε_{max}, the weight function between the particles i and j subjected to fracture is set to zero, Eq. 47. Thus the connection between the particles is lost, characterizing the brittle fracture point of the solid.

$$\varepsilon_{ij} > \varepsilon_{max} \Longrightarrow w(|\boldsymbol{r}_{ij}|) = 0 \tag{47}$$

To avoid problems of overlapping among fractured particles, that subsequently can collide each other, a more generic contact detection algorithm is proposed herein.

Initially the particles that forms the solids are divided into surface and internal particles. Similar to the condition of free surface for fluid [Koshizuka and Oka (1996)], the particle number density n_i is used as criterion. If the value of n_i is lower than a certain value, Eq. 48, the particle is classified as a solid surface particle.

$$n_i < n_i^{max} - n_c \tag{48}$$

where n_i^{max} is the maximum value of particle number density and n_c is a constant value. In the present work $n_c = 0.5$ is adopted.

This reclassification of the solid particle in surface particle and internal particle is carried out in every time step.

In practice, for each particle i, the weight functions between the particle i and its initial neighboring particles are stored in a matrix, together the index of neighbor particles. In case of fracture of a internal solid particle i and its neighbor j, since the distance between them increases, their particle number density decrease. As a result, they are reclassified as surface particles, as shown in Fig. 1, and the weight function between the particles i and j is set to zero. As rebinding of fractures surfaces is not considered in the present study, once a solid particle is classified as surface one, it is not reversible.

In order to check the occurrence of collision between a pair of surface particles, the relationship and the weight function between the particles are checked first. If

Figure 1: Surface particles (red) and internal particles (orange) during fracture.

the pair of surface particles are neighbors and the weight function is different of zero, it means that they are adjacent particles on the surface of a solid. Then the pair of particles are treated like internal particles and no special treatment for the collision is performed. In case the particles are neighbors and the weight between them is zero, the interaction between the pair of particles is taken into account when the distance between them is less than the initial distance l_0, i.e., when they are in compression. This results in repulsive forces acting between the particles. By applying this collision check and treatment, new surface particles associated to the newly formed solid surface due fracture can be detected dynamically, so that overlapping of surface particles belonging to different surfaces can be avoided, as well as overcoming the problem of misdetection of a pair of adjacent particles of a solid surface as particles that belong to two distinct surfaces in collision.

4.5 Fluid-structure interaction

In case of fluid-structure interaction, a partitioned weak coupling is adopted. When solving the fluid motion, the solid surface particles are treated like a fluid particle and their pressures are computed by solving Poisson equation for the pressure (Eq. 23), together with the fluid particles. After that, the calculated pressure field of the solid surface particles and its neighboring fluid particles is taken into account to determine the motion of elastic solid by rewritten the momentum (Eq. 5) for solid surface particles as:

$$\rho \frac{D\boldsymbol{v}}{Dt} = \nabla \cdot (\boldsymbol{\sigma} - p\boldsymbol{I}) + \boldsymbol{b} + \boldsymbol{F}_{fs} \tag{49}$$

where the body force vector $\boldsymbol{F}_{fs}$ is calculated using the average pressure of the particles i and j^* as:

$$\boldsymbol{F}_{fs} = \frac{2d}{\tilde{n}_i} \sum_{j^* \neq i} \frac{P_{ij^*}}{|\boldsymbol{r}_{j^*} - \boldsymbol{r}_i|^2} (\boldsymbol{r}_{j^*} - \boldsymbol{r}_i) w(|\boldsymbol{r}_{ij}|) \tag{50}$$

where $P_{ij*} = (P_i + P_{j*})/2$ and $j*$ represents fluid and solid surface particles in the neighborhood of the particle i, excluding the dummy particles.

$\tilde{n}_i$ is the particle number density computed considering only the neighborhood fluid and solid surface particles. For a solid surface particle i, $\tilde{n}_i$ can be obtained by subtracting its initial particle number density calculated considering only solid particles $(n_i^0)_{solid}$ from the particle number density calculated considering all of its neighbor particles $(n_i)_{total}$:

$$\tilde{n}_i = (n_i)_{total} - (n_i^0)_{solid} \tag{51}$$

Fig. 2 shows the coupling between the fluid and solid particles. Only fluid and solid surface particles (blue + brown) within the neighborhood range r_e are considered for the calculation of the force $\boldsymbol{F}_{fs}$ on the solid surface particles (brown) while the solid particles (orange) within the neighborhood range r_e are neglected.

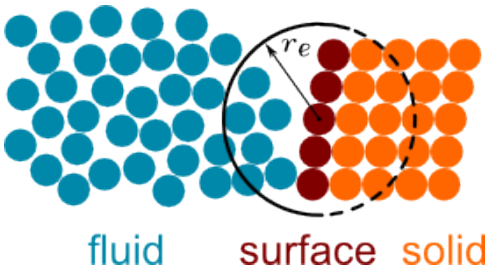

Figure 2: The interaction among fluid, solid surface and solid particles.

On the other hand, to complete the coupling between solid and fluid, the displacement and velocity of elastic solid are used as the boundary conditions of the fluid. This procedure is repeated for each time step.

4.6 Numerical stability

In order to avoid numerical instabilities, stability criteria should be satisfied in the simulations. An important stability criterion utilized in Computational Fluid Dynamics is the CFL condition [Courant, Friedrichs, and Levy (1967)]. The CFL condition adopted in this work is given by the following equation:

$$\Delta t < \frac{l_0 C}{|v|_{max}}, \quad 0 < C \leq 1 \tag{52}$$

where, Δt is the time step, $|v|_{max}$ the maximum velocity and C the Courant number.

A relevant aspect of the coupling algorithm is the time steps of fluid Δt_f and solid Δt_s. The transient response for each material has a different time scales and in most cases the CFL condition requires a much smaller time step for elastic solid than incompressible flow. To avoid the use of very small time step for the fluid domain, which is much more time consuming due to the solution of the system of Poisson equation for the pressure (Eq. 22), and increasing computational cost, a sub-cycling algorithm of elastic solid is adopted during the simulation.

5 Results and discussions

In order to evaluate the performance of the method, several example simulations are carried out. First, a cantilever beam is simulated and the maximum displacement and the natural frequency obtained by the numerical simulation are compared to analytical results, allowing to verify the convergence of the method. After that, the simulations of a collision between two elastic solids are carried out without and with the proposed contact detection algorithm to show the improvement when involving brittle fracture. Finally, two FSI problems are analyzed. The first case presents a dam-break problem, where the collapsing water column hits a fixed elastic plate and horizontal displacements obtained by the numerical simulations are compared with results available in the literature, obtained by other numerical methods. The second case consists of liquid sloshing inside a rectangular tank with a fixed elastic plate. For this case two filling levels are considered. The horizontal displacements of the elastic plate obtained by numerical simulations are compared to the results provided by the experiment performed by Idelsohn, Marti, Souto-Iglesias, and Onate (2008b).

5.1 Cantilever beam

As a simple dynamic case, the first mode shape of a cantilever beam of length $l = 2.0\,m$ with square cross section $b = 0.1\,m$, is considered. The material properties are density $\rho = 1000\ kg/m^3$, Young's modulus $E = 100\ MPa$ and Poisson's ratio $\nu = 0.3$. In order to investigate the convergence of the method, different distance of particles (dp) are considered $dp = 20.00$, 10.00, 5.00, 2.50 and 1.25 mm, with ratio $b/dp = 5$, 10, 20, 40 and 80. All cases are simulated with time step $\Delta t = 10^{-6}\ s$. The computed results are compared to analytical results of maximum amplitude Δ_{max} and natural frequency f, approximated by Eq. 53 and Eq. 54, respectively.

$$\Delta_{max} = \frac{\rho g A l^4}{8EI} \tag{53}$$

$$f = \frac{1.875^2}{2\pi}\sqrt{\frac{EI}{\rho A l^4}} \tag{54}$$

where A is the cross section area.

The plotted results of displacement can be seen in the graphic presented in Fig. 3 and the results of natural frequency, maximum amplitude and discrepancy between computed results and analytical results of maximum amplitude, for the first mode shape, are shown in Tab. 1.

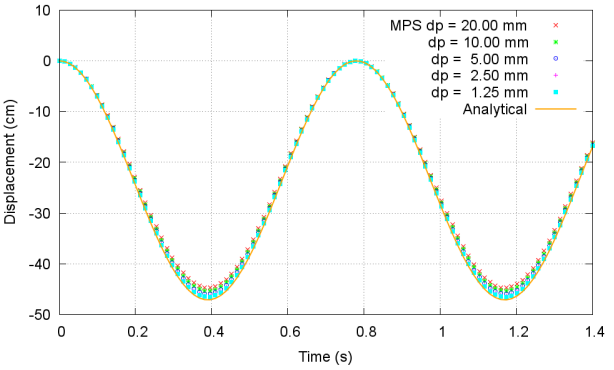

Figure 3: Maximum deflection of the cantilever beam.

Table 1: Results of the convergence test for the cantilever beam.

Model	b/dp	f (Hz)	Δ_{max} (cm)	Discrepancy (%)
MPS ($dp = 20.00\ mm$)	5	1.27	44.70	5.07
MPS ($dp = 10.00\ mm$)	10	1.27	45.30	3.80
MPS ($dp = 5.00\ mm$)	20	1.27	45.90	2.53
MPS ($dp = 2.50\ mm$)	40	1.27	46.27	1.74
MPS ($dp = 1.25\ mm$)	80	1.27	46.45	1.36
Analytical solution	-	1.27	47.09	-

Results of natural frequency obtained by the simulations show excellent agreement compared with the analytical solution. The computed maximum amplitude shows a good agreement with analytical solutions, especially for $dp = 1.25\ mm$, ratio $b/dp = 80$, with relative discrepancy about 1.36%. Also, the results show convergence of the numerical approach for the dynamic simulation. Even for the roughest case of the relatively long elastic beam considered herein, with $b/dp = 5$, the discrepancy of the maximum deflection is about 5.00%.

5.2 Brittle fracture simulation

Fig. 4 shows initial conditions of the case of collision between two elastic solids involving brittle fracture. A cube (magenta) 0.5 x 0.5 x 0.5 m with initial velocity $v_y = -15\ m/s$ collides a block (blue) 1.0 x 0.25 x 2.0 m initially without motion. The material properties of the cube are density $\rho = 1000\ kg/m^3$, Young's modulus $E = 6\ MPa$ and Poisson's ratio $\nu = 0.3$ and the material properties of the block are density $\rho = 1000\ kg/m^3$, Young's modulus $E = 10\ MPa$ and Poisson's ratio $\nu = 0.3$. The simulation parameters are particle distance $dp = 0.05\ m$ and time step $\Delta t = 10^{-6}\ s$. The critical distance of fracture is $\varepsilon_{max} = 0.2$.

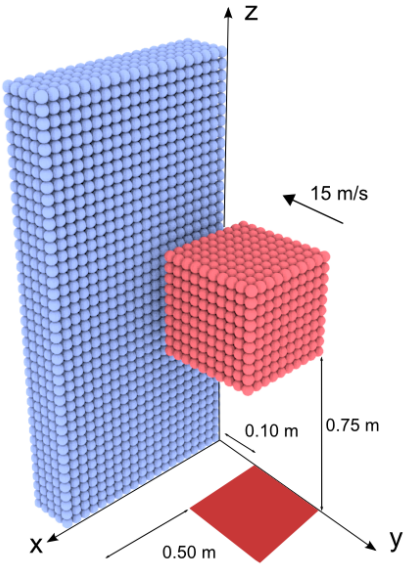

Figure 4: Initial conditions of the case of collision.

Fig. 5 gives the snapshots of the relevant instants of the simulations. The left and the right columns show, respectively, fracture without and with the proposed contact detection. The collision of two elastic solids occur at 0.07 s. After the fracture occurs in the left side of the block at 0.60 s, the collision between the newly formed fracture surfaces is detected at 0.70 s. The repulsion due to collision between particles of fractured surface is visible in the case with contact detection at 1.00 s. As a result, the parts of block move away from each other. Meanwhile as shown in the left column of Fig. 5, if collision detection between the surface created by fracture is not performed, a new and stronger collision between the fractures surfaces occurs

at 1.70 *s*. Due of the absence of collision detection and treatment of the fracture surfaces, the simulation diverged owing to the overlap of the particles.

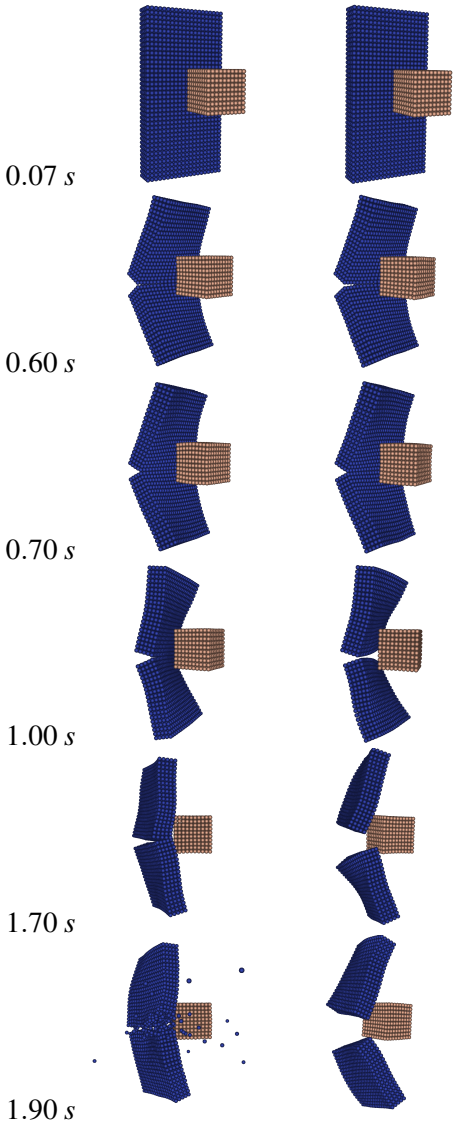

Figure 5: Snapshots of the main instants of the fracture due to collision between a cube and a block. Left: simulation carried out without the contact detection; Right: simulation carried out with the contact detection.

5.3 Dam-break on elastic plate

A dam-break problem, similar to the case investigated by Koshizuka, Tamako, and Oka (1995) using a rigid obstacle, is simulate with a fixed elastic plate, allowing the investigation of interaction between fluid and elastic solid. The initial configuration of the problem is shown in Fig. 6. The dimensions of elastic plate, which is highlighted in orange, are 12.0 x 80.0 *mm*. The physical properties of the elastic solid are: density $\rho = 2500\ kg/m^3$, Young's modulus $E = 1\ MPa$ and Poisson's ratio $v = 0.0$. The physical properties of the fluid are: density $\rho = 1000\ kg/m^3$ and kinematic viscosity $\nu = 10^{-6}\ m^2/s$. As simulation parameters, the values in Tab. 2 are considered. The simulations are performed for 2 *s*.

Table 2: Dam-break on elastic plate. Simulation parameters.

dp (mm)	Δt_{fluid} (s)	Δt_{solid} (s)	Fluid particles	Solid particles
3.00	10^{-4}	10^{-6}	4656	108
1.50	10^{-4}	10^{-6}	19208	440
0.50	10^{-5}	10^{-6}	170527	3840

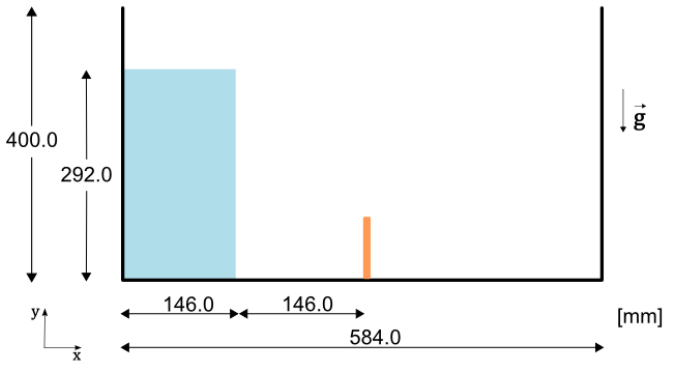

Figure 6: Dimensions and initial conditions of dam-break on elastic plate.

Fig. 7, Fig. 8 and Fig. 9 show the time history of the horizontal displacement of the top of the elastic plate obtained by the present simulation with $dp = 3.00$, 1.50 and 0.50 *mm*, respectively, and the results of the others methods available in the literature [Walhorn, Kolke, Hubner, and Dinkler (2005); Marti, Idelsohn, Limache, Calvo, and D'Elia (2006); Idelsohn, Marti, Limache, and Onate (2008a); Amanifard, Hesan, and Rahbar (2011)]. Comparing the result obtained by the present

simulation with those from other methods, it may be noted that initially all of the results has the same tendency. The maximum displacement of 4.1 *cm* of the present simulation is almost identical to that obtained by FEM and SPH, but slightly lower than the results from PFEM computations. For $dp = 3.00\ mm$, after the instant 0.4 *s* the displacement obtained by the present simulation remains in 2.1 *cm*, higher than the results of the others methods. From 0.6 *s* the oscillating behavior of the curve resembles the curve of SPH, but with differences in displacement amplitudes. For $dp = 1.50\ mm$, after the instant 0.4 *s* the displacement obtained by the present simulation remains in 1.7 *cm* which is similar to the results from SPH and PFEM simulations. From 0.6 *s*, the curve shows less vibration cycles and the obtained result is relatively close to the SPH result. Finally, the simulation with $dp = 0.50\ mm$ presents distinct decreasing curve from the other two simulations without concavity between the instants 0.3 *s* and 0.6 *s*, reaching a value of 1.7 *cm* at the instant 0.6 *s*. After the instant 0.6 *s*, two peaks of -1.1 *cm* followed by a peak of 1.1 *cm* and another peak -0.9 *cm* are computed. Each numerical method exhibit slightly distinct oscillating behavior and the displacement calculated by the present simulation based on the MPS method shows less vibration cycles. Also, the obtained result is relatively close to the SPH result. In addition to this, the oscillations tend to a point of equilibrium between fluid and structure due to the damping of elastic plate on the fluid.

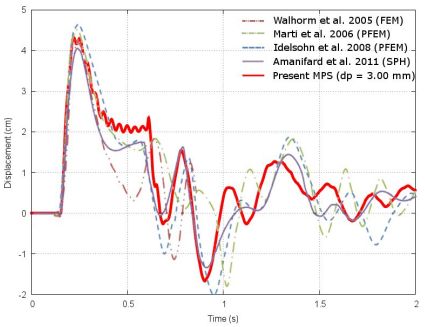

Figure 7: Horizontal displacement of the elastic plate $dp = 3.00\ mm$.

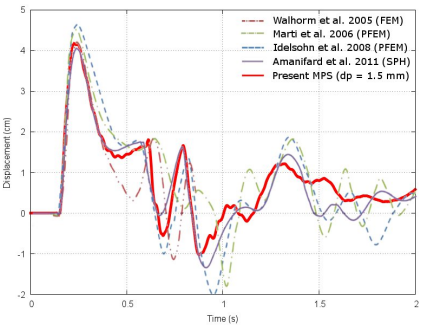

Figure 8: Horizontal displacement of the elastic plate $dp = 1.50\ mm$.

Fig. 10 shows a sequence of frames from the simulation obtained by SPH [Rafiee and Thiagarajan (2009)], PFEM [Idelsohn, Marti, Limache, and Onate (2008a)] and the simulations carried in the present study. It can be observed a good agreement between the methods. As there are no experimental results of the present case, taking into account the physics of the problem, the results show that, compared

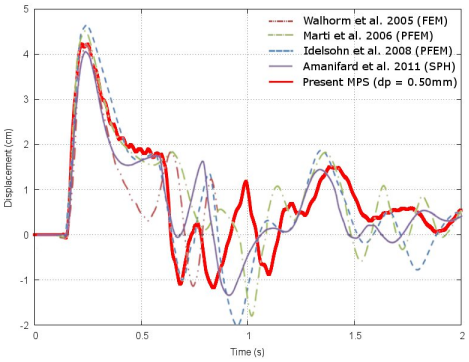

Figure 9: Horizontal displacement of the elastic plate $dp = 0.50\ mm$.

with the methods currently available, the present approach is also able to reproduce the main behaviors of the problems involving free surface flow and elastic solids.

5.4 Sloshing with an elastic plate

The case consists of a rectangular tank partially filled with oil, and an elastic plate fixed at the midpoint of the tank bottom. It is a 2D experiment performed by Idelsohn, Marti, Souto-Iglesias, and Onate (2008b). The dimensions and initial configuration of the experiment are illustrated in Fig. 11. The tank is subjected to a oscillatory motion of amplitude $\alpha = 4°$, around the midpoint of the bottom, and period T obtained by the following equation:

$$T = 2\pi \left(\sqrt{\frac{\pi g}{L} tanh\left(\frac{\pi H_L}{L}\right)} \right)^{-1} \tag{55}$$

where L is the tank length and H_L is the filling level.

Two filling levels are considered and the horizontal displacements of the elastic plate obtained by numerical simulations are compared to the experimental measurements. The horizontal displacement (x) of the elastic plate is relative to the local reference frame fixed to the tank, Fig. 12.

It should be noted the initial differences between the experiment and numerical simulation due to the inertia of the tank. In the experiment, the transition from initial static state to harmonic motion occurs gradually, while in the numerical simulation, this transition is instantaneous. Thus, in the early stages, the experimental measurement and the numerical results are different. In order to compare the results disregarding the transient responses, the results obtained by the present simulation

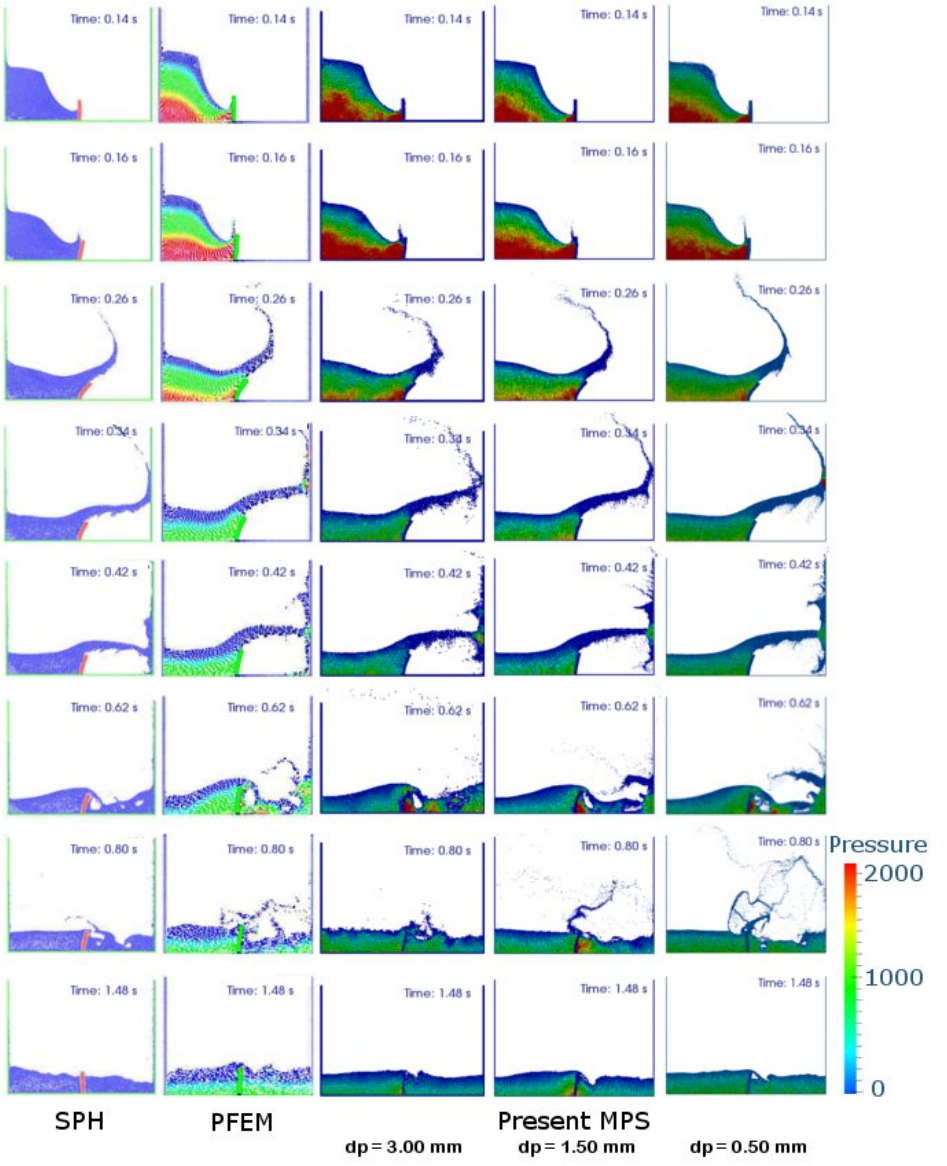

Figure 10: Dam-break on elastic plate: comparison between SPH [Rafiee and Thiagarajan (2009)], PFEM [Idelsohn, Marti, Limache, and Onate (2008a)] and present MPS (0.14 s, 0.16 s, 0.26 s, 0.34 s, 0.42 s, 0.62 s, 0.80 s, 1.48 s).

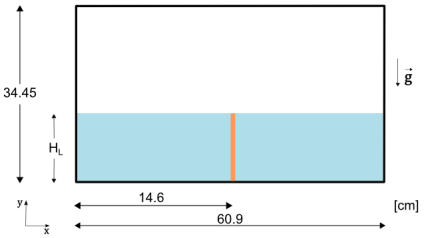

Figure 11: Dimensions and initial conditions of sloshing.

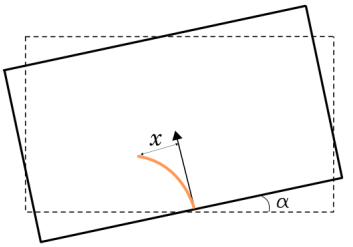

Figure 12: Local reference frame fixed to the tank.

are shifted in time to match the first peak of the experimental and numerical results after achieving steady state.

5.4.1 Elastic plate immersed in low filling

The tank is filled to $H_L = 57.4\ mm$ and subjected to a oscillatory motion of period $T = 1.646\ s$. The dimensions of elastic plate, which is highlighted in orange color, Fig. 11, are 4.0 x 57.4 *mm* and the physical properties are: density $\rho = 1100\ kg/m^3$, Young's modulus $E = 6\ MPa$ and Poisson's ratio $v = 0.49$. The physical properties of the fluid are: density $\rho = 917\ kg/m^3$ and kinematic viscosity $\nu = 5x10^{-5}\ m^2/s$. As simulation parameters, the values in Tab. 3 are considered. The simulations are performed for 10 *s*.

Table 3: Elastic plate immersed in low filling. Simulation parameters.

dp (mm)	Δt_{fluid} (s)	Δt_{solid} (s)	Fluid particles	Solid particles
1.00	10^{-5}	10^{-6}	34485	228
0.80	10^{-5}	10^{-6}	54432	360
0.50	10^{-5}	10^{-7}	139150	920

Fig. 13 gives the computed time history and the measured results of the horizontal displacement of the top of the elastic plate. Due to the differences in excitation in the early stages of the experiment and numerical simulation, as mentioned above, the experimental values have a displacement of 0.12 *cm* at 0.48 *s* and -0.47 *cm* at 0.92 *s*, while the numerical result presents a displacement of -0.8 *cm* at 1.00 *s*. After the instant 1.00 *s*, the period of oscillation of the elastic plate is, approximately, 1.70 *s* for both experimental values and numerical results. Between the instants 1.00 *s* and 7.00 *s*, the measured magnitude of the crest and valley of the displace-

ment are different with respect to undeformed condition of the elastic plate. On the other hand, for the computed result, this symmetry is observed.

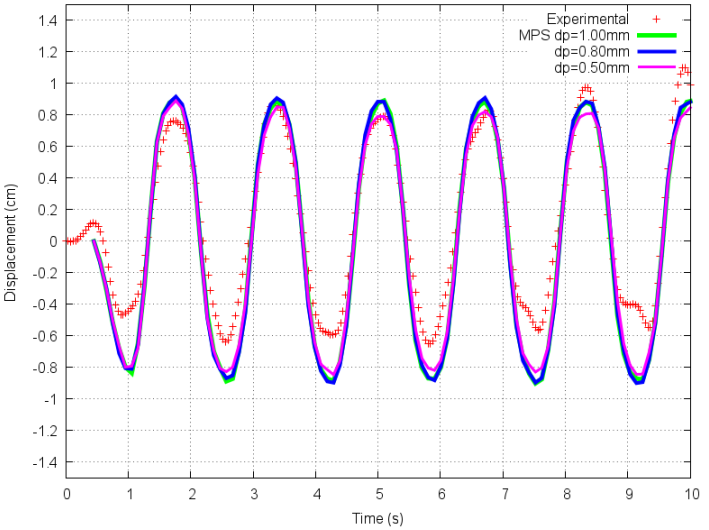

Figure 13: Horizontal displacement of the elastic plate immersed in low filling. Results of present MPS simulations and the experimental measurements [Idelsohn, Marti, Souto-Iglesias, and Onate (2008b)].

Table 4: Elastic plate immersed in low filling. Results of present MPS simulations and the experimental measurements [Idelsohn, Marti, Souto-Iglesias, and Onate (2008b)].

dp (mm)	Experimental (cm)	Present MPS (cm)	Error (%)
1.00	1.44	1.83	27.08
0.80	1.44	1.84	27.78
0.50	1.44	1.71	18.75

The error of the computed is evaluated between 1.72 s and 6.76 s, which is the interval when experiment reached the steady state and remains stable. The error is defined as the ratio between the modulus of the difference between average amplitudes of the experimental measurement and numerical simulation by average amplitudes obtained experimentally. Tab. 4 shows the errors for particle distance $dp = 1.00$, 0.80 and 0.50 mm. When particle distance are 1.00 and 0.80mm, the

Figure 14: Elastic plate immersed in low filling. Comparison between present MPS simulations and experiment [Idelsohn, Marti, Souto-Iglesias, and Onate (2008b)] (0.90 s, 1.20 s, 1.67 s, 2.07 s, 2.47 s, 2.87 s, 3.33 s, 3.76 s).

error is relatively large achieving 27%. However, for particle distance 0.50mm, the error reduces to 18.75%.

Fig. 14 shows a sequence of frames from the present MPS simulations and experiment. It can be observed a similar behavior between the experiment and the present MPS simulations.

5.4.2 Elastic plate immersed in high filling

The tank is filled to $H_L = 114.8\ mm$ and subjected to a oscillatory motion of period $T = 1.211\ s$. The dimensions of elastic plate, which is highlighted in orange, Fig. 11, are 4.0 x 114.8 mm and the physical properties are: density $\rho = 1100\ kg/m^3$, Young's modulus $E = 6\ MPa$ and Poisson's ratio $v = 0.49$. The physical properties of the fluid are: density $\rho = 917\ kg/m^3$ and kinematic viscosity $\nu = 5x10^{-5}\ m^2/s$. As simulation parameters, the values in Tab. 5 are considered. The simulations are performed for 10 s.

Table 5: Elastic plate immersed in high filling. Simulation parameters.

dp (mm)	Δt_{fluid} (s)	Δt_{solid} (s)	Fluid particles	Solid particles
1.00	10^{-5}	10^{-6}	69920	460
0.80	10^{-5}	10^{-6}	108864	720
0.50	10^{-5}	10^{-7}	278300	1840

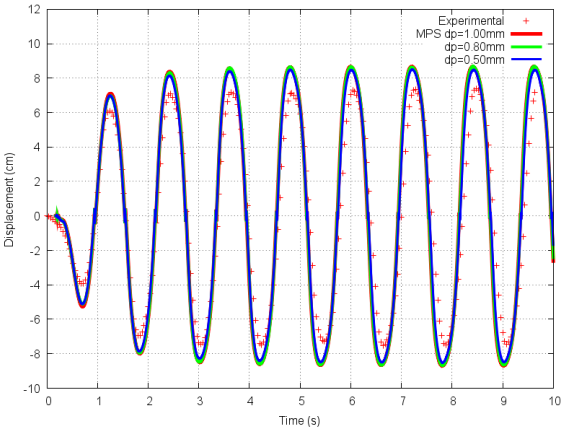

Figure 15: Horizontal displacement of the elastic plate immersed in high filling. Results of present MPS simulations and the experimental measurements [Idelsohn, Marti, Souto-Iglesias, and Onate (2008b)].

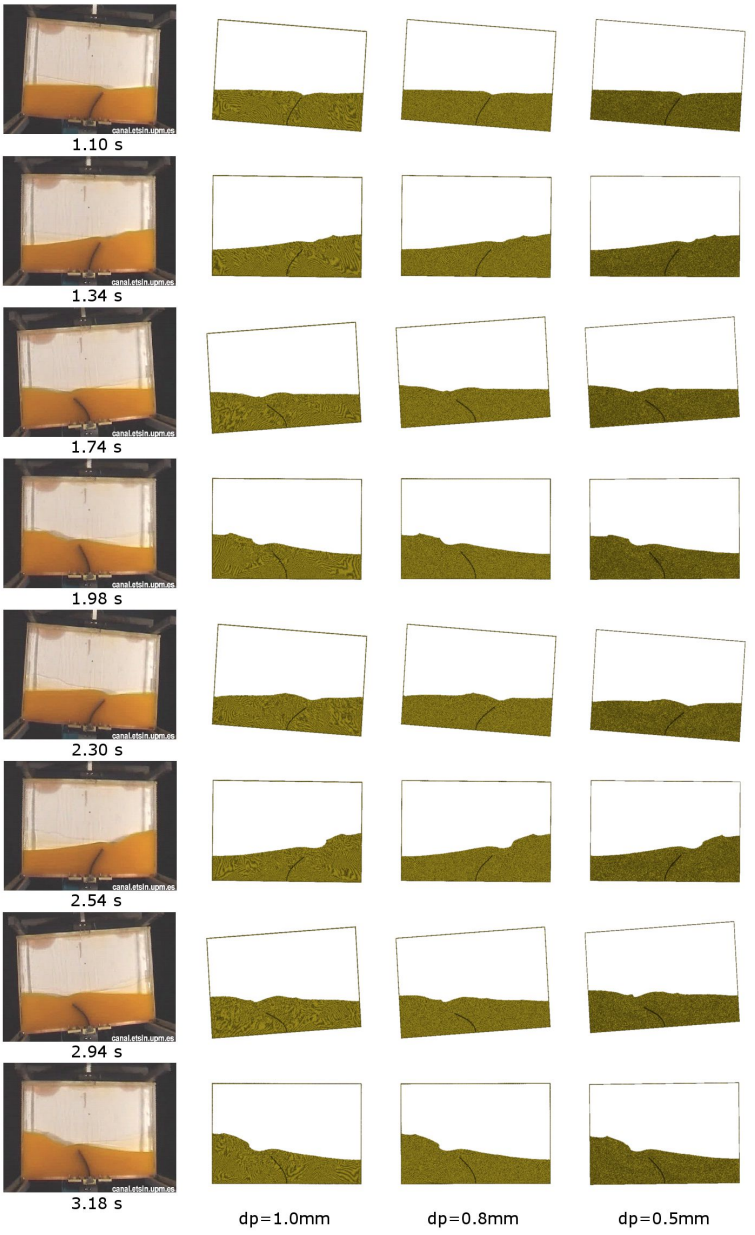

Figure 16: Elastic plate immersed in high filling. Comparison between present MPS simulations and experiment [Idelsohn, Marti, Souto-Iglesias, and Onate (2008b)] (1.10 s, 1.34 s, 1.74 s, 1.98 s, 2.30 s, 2.54 s, 2.94 s, 3.18 s).

Table 6: Elastic plate immersed in high filling. Results of present MPS simulations and the experimental measurements [Idelsohn, Marti, Souto-Iglesias, and Onate (2008b)].

dp (mm)	Experimental (cm)	Present MPS (cm)	Error (%)
1.00	14.65	17.24	17.68
0.80	14.65	17.22	17.54
0.50	14.65	16.86	15.08

Fig. 15 shows the computed time history and the measured results of the horizontal displacement of the top of the elastic plate. Similar to the former low filling case, computed results show transient behavior different from the experimental measurement because the inertia of the system is not considered in the numerical simulation. After the instant 1.00 s, the oscillation of the elastic plate becomes stable with a period of approximately 1.20 s for both experimental measurement and numerical results. The experimental measurement shows peak values around -7.52 cm and 7.38 cm, while the numerical result presents peak values around -8.70 cm and 8.70 cm. Both experiment and numerical results show that the plate oscillates symmetrically with respect to initial undeformed position of the elastic plate.

The errors evaluated from 2.44 s to 9.08 s are given in Tab. 6, for particle distance $dp = 1.00, 0.80$ and 0.50 mm. In relation to the former low filling case, the error reduced significantly and the convergence of the numerical results can also observed.

Fig. 16 shows a sequence of frames from the present MPS simulations and experiment. As in the previous case, it is again observed a similar behavior between the experiment and the present MPS simulations.

6 Concluding remarks

A computer code for the modeling and simulation of brittle fracture and hydroelastic problems has been implemented in the present work. A more generic contact detection algorithm that takes into account the presence of the solid surfaces generated by brittle fracture is proposed. To solve hydroelastic problems involving free surface, a partitioned coupling between fluid and isotropic elastic solid is adopted. Explicit and semi-implicit time integration algorithms are used for elastic solid and fluid domains, respectively. Matching of the time steps in both domains is done by sub-cycling technique to improve the computational efficiency. A dynamic case of slender cantilever beam is analyzed and the convergence of the method is verified. After that, a collision between two elastic solids with brittle fracture and further collision between the fragments is simulated showing the improvement

achieved. Finally, to validate the fluid-structure interaction simulation approach, two FSI problems are simulated and compared with other computational methods or experimental results found in literature. Comparisons with available numerical results of a dam breaking on an elastic plate are performed and it can be observed a good agreement between the results of present method and another methods, taking into account the physics of the problem. In the second case, available experimental measurements of the interactions between liquid sloshing, and an elastic plate are compared with numerical results. For the low filling case, it was noted significant errors in displacements, while in the high filling case the improvement on the accuracy can be observed. On the other hand, the convergence of the numerical results can be observed in the both filling cases. The comparisons of the results showed the effectiveness of the present approach to reproduce the main behaviors of the problems involving fracture of brittle materials and interaction between free surface flow and elastic solids.

Acknowledgement: This work had financial support from CAPES and the authors are thankful to Petrobras for financial support on the development of the simulation system based on MPS method.

References

Amanifard, N.; Hesan, M.; Rahbar, B. (2011): An SPH approach for fluid-hypoelastic structure interactions with free surfaces. In *Proceedings of the World Congress on Engineering*.

Antoci, C.; Gallati, M.; Sibilla, S. (2007): Numerical simulation of fluid-structure interaction by SPH. *Computers & Structures*, vol. 85, no. 11–14, pp. 879–890.

Bellezi, C. A.; Cheng, L. Y.; Nishimoto, K. (2013): A numerical study of the effects of bow shape on green water phenomenon. In *Proceedings of the Twenty-third (2013) International Offshore and Polar Engineering - ISOPE2013*.

Bonet, J.; Lok, T.-S. L. (1999): Variational and momentum preservation aspects of smooth particle hydrodynamic formulations. *Computer Methods in Applied Mechanics and Engineering*, vol. 180, no. 1–2, pp. 97–115.

Campbell, J. C.; Vignjevic, R.; Patel, M.; Milisavljevic, S. (2009): Simulation of water loading on deformable structures using SPH. *Computer Modeling in Engineering & Sciences*, vol. 49, no. 1, pp. 1–21.

Chen, F.; Wang, C.; Xie, B.; Qin, H. (2013): Flexible and rapid animation of brittle fracture using the smoothed particle hydrodynamics formulation. *Computer Animation and Virtual Worlds*, vol. 24, no. 3–4, pp. 215–224.

Cheng, L. Y.; Gomes, D. V.; Yoshino, A. M.; Nishimoto, K. (2011): Numerical simulation of oil leakage, water flooding and damaged stability of oil carrier based on moving particle semi-implicit (mps) method. In *Second International Conference on Particel-based Methods - Fundamentals and Applications - PARTICLES 2011*.

Cheng, L. Y.; Oliveira, L. H.; Favero, E. H.; Oliveira, I. B.; Gonçalves, O. M. (2013): Simulation of drainage system in building using particle-based numerical method. In *39th International Symposium of CIB W062*.

Chhatkuli, S.; Koshizuka, S.; Uesaka, M. (2009): Dynamic tracking of lung deformation during breathing by using particle method. *Modelling and Simulation in Engineering*.

Chikazawa, Y.; Koshizuka, S.; Oka, Y. (2001): A particle method for elastic and visco-plastic structures and fluid-structures interactions. *Computational Mechanics*, vol. 27, no. 2, pp. 97–106.

Courant, R.; Friedrichs, K.; Levy, H. (1967): On the partial difference equations of mathematical physics. *IBM Journal of Research and Development*, vol. 11, no. 2, pp. 215–234.

Das, R.; Cleary, P. (2010): Effect of rock shapes on brittle fracture using smoothed particle hydrodynamics. *Theoretical and Applied Fracture Mechanics*, vol. 53, no. 1, pp. 47–60.

Gingold, R. A.; Monagham, J. J. (1977): Smoothed particle hydrodynamics: theory and application to non-spherical stars. *Monthly Notices of the Royal Astronomical Society*, vol. 181, pp. 375–389.

Guo, Y. J.; Nairn, J. A. (2006): Three-dimensional dynamic fracture analysis using the material point method. *Computer Modeling in Engineering & Sciences*, vol. 16, no. 3, pp. 141–155.

Harlow, F. H. (1964): The particle-in-cell computing method for fluid dynamics. *Methods in Computational Physics*, vol. 3, pp. 319–343.

Idelsohn, S. R.; Marti, J.; Limache, A.; Onate, E. (2008a): Unified lagrangian formulation for elastic solids and incompressible fluids: application to fluid-structure interaction problems via the PFEM. *Computer Methods in Applied Mechanics and Engineering*, vol. 197, no. 19–20, pp. 1762–1776.

Idelsohn, S. R.; Marti, J.; Souto-Iglesias, A.; Onate, E. (2008b): Interaction between an elastic structure and free-surface flows: experimental versus numerical comparisons using the PFEM. *Computational Mechanics*, vol. 43, no. 1, pp. 125–132.

Idelsohn, S. R.; Onate, E. (2006): To mesh or not to mesh. That is the question... *Computer Methods in Applied Mechanics and Engineering*, vol. 195, no. 37–40, pp. 4681–4696.

Idelsohn, S. R.; Onate, E.; Pin, F. D. (2004): The particle finite element method: a powerful tool to solve incompressible flows with free-surfaces and breaking waves. *International Journal for Numerical Methods in Engineering*, vol. 61, no. 7, pp. 964–989.

Ikeda, H.; Koshizuka, S.; Oka, Y.; Park, H. S.; Sugimoto, J. (2001): Numerical analysis of jet injection behavior for fuel-coolant interaction using particle method. *Journal of Nuclear Science and Technology*, vol. 38, no. 3, pp. 174–182.

Ishihara, D.; Yoshimura, S. (2005): A monolithic approach for interaction of incompressible viscous fluid and an elastic body based on fluid pressure poisson equation. *International Journal for Numerical Methods in Engineering*, vol. 64, no. 2, pp. 167–203.

Isshiki, H. (2011): Discrete differential operators on irregular nodes (DDIN). *International Journal for Numerical Methods in Engineering*, vol. 88, no. 12, pp. 1323–1343.

Kakuda, K.; Ushiyama, Y.; Obara, S.; Toyotani, J.; Matsuda, S.; Tanaka, H.; Katagiri, K. (2010): Flow simulations in a liquid ring pump using a particle method. *Computer Modeling in Engineering & Sciences*, vol. 66, no. 3, pp. 215–226.

Kim, K.-S.; Lee, B.-H.; Kim, M.-H.; Park, J.-C. (2011): Simulation of sloshing effect on vessel motions by using MPS (moving particle simulation). *Computer Modeling in Engineering & Sciences*, vol. 79, no. 3, pp. 201–221.

Koshizuka, S.; Ikeda, H.; Oka, Y. (1999): Numerical analysis of fragmentation mechanisms in vapor explosions. *Nuclear Engineering and Design*, vol. 189, no. 1–3, pp. 423–433.

Koshizuka, S.; Oka, Y. (1996): Moving-particle semi-implicit method for fragmentation of incompressible fluid. *Nuclear Science and Engineering*, vol. 123, no. 3, pp. 421–434.

Koshizuka, S.; Tamako, H.; Oka, Y. (1995): A particle method for incompressible viscous flow with fluid fragmentation. *Computational Fluid Dynamics Journal*, vol. 4, no. 1, pp. 29–46.

Lee, B.-H.; Jeong, S.-M.; Hwang, S.-C.; Park, J.-C.; Kim, M.-H. (2013): A particle simulation of 2-D vessel motions interacting with liquid-sloshing cargo. *Computer Modeling in Engineering & Sciences*, vol. 91, no. 1, pp. 43–63.

Lee, B.-H.; Park, J.-C.; Kim, M.-H. (2010): Two-dimensional vessel-motion/liquid-sloshing interactions and impact loadings by using a particle method. In *Proceedings of the ASME 2010 29th International Conference on Ocean, Offshore and Arctic Engineering - OMAE2010*.

Lee, B.-H.; Park, J.-C.; Kim, M.-H.; Hwang, S.-C. (2011): Moving particle simulation for mitigation of sloshing impact loads using surface floaters. *Computer Modeling in Engineering & Sciences*, vol. 75, no. 2, pp. 89–112.

Lucy, L. (1977): A numerical approach to the testing of the fission hypothesis. *Astronomical Journal*, vol. 82, pp. 1013–1024.

Marti, J.; Idelsohn, S. R.; Limache, A.; Calvo, N.; D'Elia, J. (2006): A fully coupled particle method for quasi-incompressible fluid-hypoelastic structure interactions. *Asociacion Argentina de Mecanica Computacional*, vol. 25, no. 9, pp. 809–827.

Motezuki, F. K.; Cheng, L. Y. (2013): Coupled particle based simulation of concrete casting and thermal diffusion. In *Proceedings of the Fourteenth International Conference on Civil, Structural and Environmental Engineering Computing*.

Nagayama, K.; Honda, K. (2012): 3d particle simulations of deformation of red blood cells in micro-capillary vessel. *Fluid Dynamics, Computational Modeling and Applications*, pp. 463–474.

Park, S.; Jeun, G. (2011): Coupling of rigid body dynamics and moving particle semi-implicit method for simulating isothermal multi-phase fluid interactions. *Computer Methods in Applied Mechanics and Engineering*, vol. 200, no. 1–4, pp. 130–140.

Rafiee, A.; Thiagarajan, K. P. (2009): An SPH projection method for simulating fluid-hypoelastic structure interaction. *Computer Methods in Applied Mechanics and Engineering*, vol. 198, no. 33–36, pp. 2785–2795.

Shakibaeinia, A.; Jin, Y.-C. (2010): A weakly compressible MPS method for modeling of open-boundary free-surface flow. *International Journal for Numerical Methods in Fluids*, vol. 63, no. 10, pp. 1208–1232.

Shibata, K.; Koshizuka, S.; Sakai, M.; Tanizawa, K. (2012): Lagrangian simulations of ship-wave interactions in rough seas. *Ocean Engineering*, vol. 42, pp. 13–25.

Song, M.; Koshizuka, S.; Oka, Y. (2003): Dynamic analysis of elastic solids by mps method. In *International Conference on Global Environment and Advanced Nuclear Power Plants*.

Sulsky, D.; Chen, Z.; Schreyer, H. L. (1994): A particle method for history-dependent materials. *Computer Methods in Applied Mechanics and Engineering*, vol. 118, no. 1, pp. 179–196.

Tsukamoto, M. M.; Cheng, L. Y.; Nishimoto, K. (2011): Analytical and numerical study of the effects of an elastically-linked body on sloshing. *Computers & Fluids*, vol. 49, no. 1, pp. 1–21.

Walhorn, E.; Kolke, A.; Hubner, B.; Dinkler, D. (2005): Fluid-structure coupling within a monolithic model involving free surface flows. *Computers & Structures*, vol. 83, no. 25–26, pp. 2100–2111.

Xiao, Y.; Han, X.; Hu, D. (2011): A coupling algorithm of finite element method and smoothed particle hydrodynamics for impact computations. *Computer Modeling in Engineering & Sciences*, vol. 23, no. 1, pp. 9–34.